

Toward Carnot efficient high output power heat engines using bubbly two-phase flow
Dror Miron^{1,3,4,*}, Yuval Neumann^{1,3,4}, Joseph Cassell^{3,4}, Nir Feintuch^{2,3}, Alexey Shinkarenko³,
and Carmel Rotschild^{1,2,3,**}

¹The Nancy and Stephen Grand Technion Energy Program, Technion – Israel Institute of Technology, Haifa 3200003, Israel

²Faculty of Mechanical Engineering, Technion – Israel Institute of Technology, Haifa 3200003, Israel

³Lava Power LTD.

*Correspondence: sdmiron@campus.technion.ac.il

**Correspondence: carmelr@technion.ac.il

⁴These authors contributed equally.

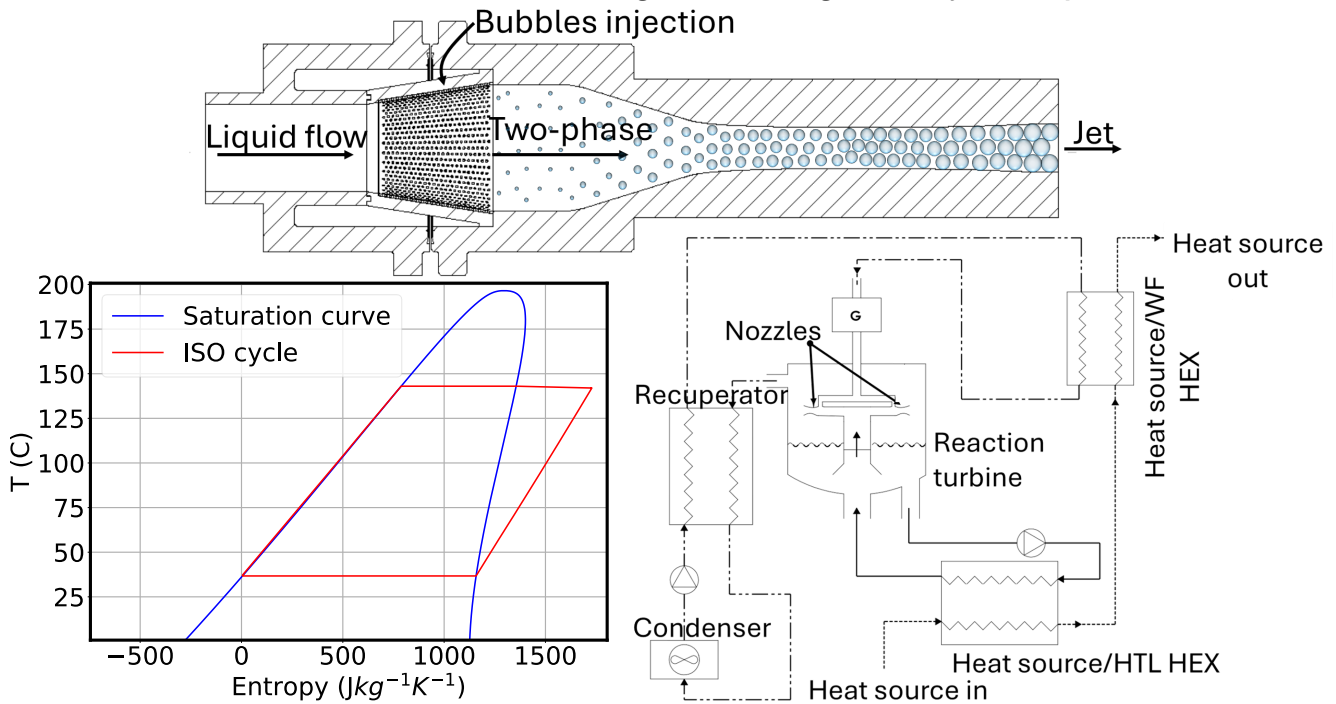
SUMMARY

Thermodynamic gas power cycles achieving Carnot efficiency require isothermal expansion, which is associated with slow processes and results in negligible power output. This study proposes a practical method for rapid near-isothermal gas expansion, facilitating efficient heat engines without sacrificing power. The method involves bubble expansion in a heat transfer liquid, ensuring efficient and near-isothermal heat exchange. The mixture is accelerated through a converging-diverging nozzle, converting thermal energy into kinetic energy. A novel organic vapor cycle employing isothermal expansion utilizing these nozzles is suggested to harness low-grade heat sources. Nozzle experiments with air and water yielded a polytropic index < 1.052 , enabling up to 71% more work extraction than adiabatic expansion. Simulations on a small-scale heat engine indicate that utilizing these nozzles for thrust generation enables decreasing heat transfer irreversibilities in the cycle, consequently resulting in up to 19% higher power output than the organic Rankine cycle using Pentane. This work paves the way for an efficient and high-power heat-to-power solution.

Graphical abstract

26

Toward Carnot Efficient Heat Engines Using Bubbly Two-phase Flow



27

KEYWORDS

28

Isothermal expansion, Heat engine, Waste heat recovery, Carnot efficiency, Two-phase nozzle

29

INTRODUCTION

30

To limit global warming corresponding to international goals, global greenhouse gas emissions should be urgently reduced¹. One of the promising methods to limit greenhouse gas emissions is by improving energy efficiency. As 72% of global primary energy production is lost to waste heat², there is great potential for energy to be sourced from waste heat recovery methods. Much of this potential lies in industrial applications, where heat is dissipated as a by-product in tens to hundreds of kilowatts. These heat sources may be available as low-grade heat in temperatures $<200^{\circ}C$, for which available heat engines are inefficient and expensive.

31

32

33

34

35

36

37

Due to its enhanced thermodynamic performance, power systems based on the organic Rankine cycle (ORC) have been considered promising for waste heat^{3,4} and geothermal energy recovery systems⁵. Therefore, improving ORC systems' performance received research attention in recent years⁶⁻¹¹. Specifically, it has been suggested to implement quasi-isothermal expansion as an alternative to adiabatic expansion since more work can be extracted^{7,12}. For example, studies indicated a flooded-expansion method to achieve quasi-isothermal expansion^{7,13,14}. Such cycles involve flooding the expansion device (screw or scroll expander) with a liquid that is in thermal equilibrium with the working fluid (WF). The liquid acts as a heat reservoir for the expanding vapor, which allows it to maintain its temperature during the expansion process. The isothermal expansion also produces super-heated vapor at the expander outlet, facilitating internal regeneration normally unavailable in conventional ORC¹⁴. Although promising, studies investigating flooding the screw expander found no change to the outlet temperature

38

39

40

41

42

43

44

45

46

47

48

49

(i.e., isothermal expansion has not been achieved) and a decreased trend of the cycle efficiency when increasing the flooding ratio^{7,8,15}. The scroll expander showed deteriorating performance when increasing the flooding ratio due to pressure drop in the scroll expander inlet^{12,16}. Another challenge mentioned in this configuration is phase separation after the expander. Consequently, a practical approach has yet to be known for realizing quasi-isothermal expansion in organic cycles.

In contrast to expander flooding, studies in marine propulsion have proposed employing air bubble expansion within water to achieve isothermal expansion. This method significantly increases the contact area between the fluids and facilitates efficient heat transfer. Additionally, this method substantially elevates the liquid-to-gas mass ratio relative to the liquid flooding technique, promoting gas expansion within a heat reservoir. Integrating these effects in a converging nozzle has enhanced thrust by allowing more effective work extraction compared to single-phase air ramjets^{17–19}. To further augment thrust, it has been proposed that choked flow conditions be attained. As such, a converging-diverging nozzle has been studied and experimented with, demonstrating supersonic flow and thrust enhancement²⁰.

This study presents the development of an efficient, high-power heat engine based on a novel thermodynamic vapor cycle incorporating quasi-isothermal expansion of bubbles in a heat transfer liquid (HTL). The large bubbles' surface area supports efficient heat transfer between the phases, and the substantial mass and heat capacity discrepancies between the phases facilitate minimal temperature drop, thereby implementing a quasi-isothermal process. The two-phase mixture flows through converging-diverging nozzles, converting the thermal energy to thrust, which rotates a reaction turbine. To this end, we combine pressure measurements and computational fluid dynamic (CFD) analysis of a two-phase flow in a converging-diverging nozzle to extract an upper boundary for the polytropic index of air. We thereby quantify the work enhancement of the near-isothermal compared to adiabatic expansion. Building on this, we simulate the performance of a heat engine that integrates the nozzles as expanders to drive a reaction turbine for electricity generation from a constant-temperature heat source. The results highlight the potential of this design, as a polytropic index of air $n < 1.052$ is determined, resulting in work extraction $>89\%$ of the isothermal work. Assuming turbine efficiencies of 75%, the proposed heat engine produces up to 10.8% greater power output than an ORC-based counterpart for 100–190 °C. Since the turbine's practical efficiency is obscure, we demonstrate that the turbine efficiencies between 70% and 90% yield an improvement of 3.2% and 33.8%, respectively, compared to the ORC heat engines at the temperature of 190 °C. These findings provide a basis for developing efficient heat engines tailored to low-grade constant temperature heat source applications.

RESULTS AND DISCUSSION

Nozzle design

The nozzle is designed according to a previously developed model for two-phase flow in a converging-diverging nozzle²¹. The design is based on the homogenous model of a bubbly mixture flowing in the nozzle, which was shown valid by others^{17,18,22–24}. Under this model, we assume that the phases are in pressure, temperature, and velocity equilibrium. The geometry of the cross-section is selected as circular. In contrast to the propulsion nozzle, where the pressure at the injection chamber is dictated and limited by the cruise velocity, the inlet pressure is a free parameter controlled by a pump, which results in supersonic flow. To illustrate the physical principle and evaluate the expansion, we introduce air into a water stream at ambient temperature. The injection pressure at the design point was chosen to be 6 bar, an air mass flow rate of 13.1

g/s , an injection temperature of $26\text{ }^{\circ}C$, and a water volumetric flow rate of $14.6\text{ }m^3/hr$. The nozzle is designed to implement a constant dp/dt to ease the heat transfer between the phases. Figure 1 shows a schematic representation of the designed nozzle.

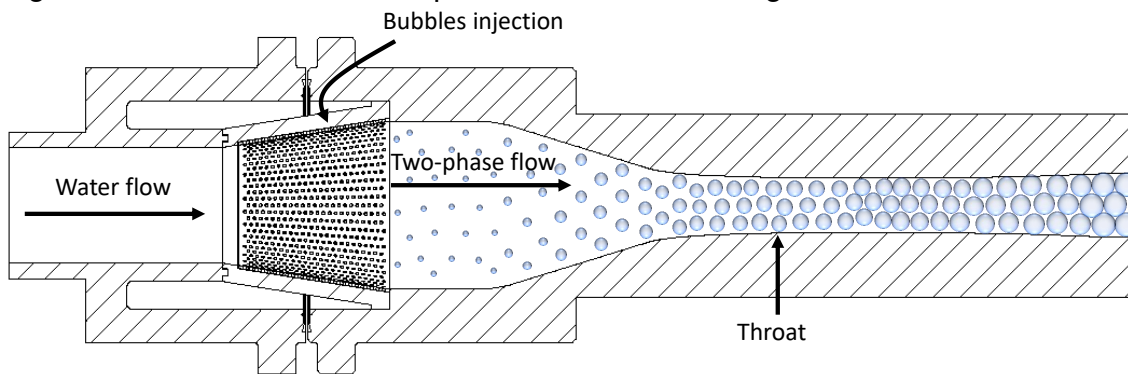
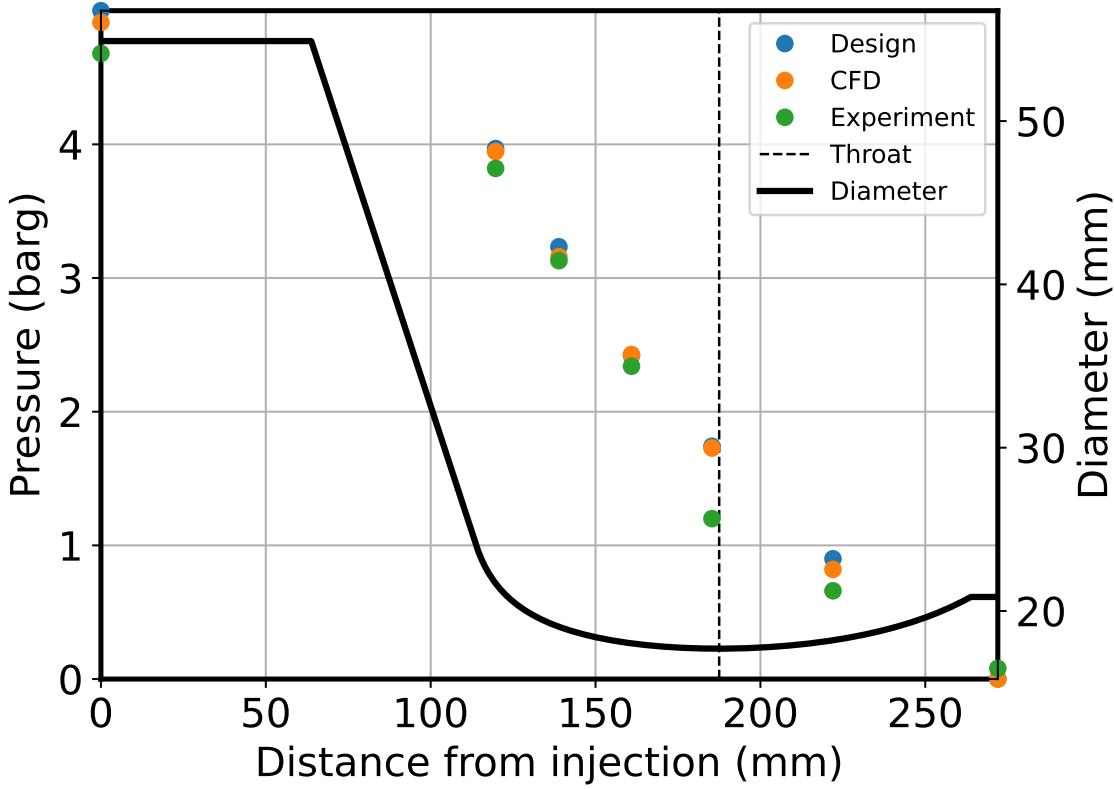


Figure 1. Nozzle design drawing

Near-isothermal expansion

During the experiments, static pressure was measured at the nozzle's injection, outlet, and other locations along the nozzle. Figure 2 presents the pressure distribution and the nozzle's diameter in the nozzle (solid black curve). It indicates that supersonic conditions are met in the nozzle since the pressure continues to drop after the throat until it reaches atmospheric pressure at the nozzle's outlet. This pressure distribution matches the nozzle's design, i.e., reducing the pressure from a 6 bar in the air injection chamber to atmospheric pressure in the nozzle's outlet. Since isothermal expansion was assumed in the nozzle's design, this is the first reinforcement of our isothermal process assumption. We note that the pressure measurement at the throat stands out, where the measured pressure is considerably lower than anticipated. We ascribe this discrepancy to the high throat sensitivity to manufacturing flaws, slip²⁵, and tap diameter²⁶ due to high pressure and velocity gradients in this region. A computational fluid dynamics (CFD) simulation was performed to analyze the anticipated pressure distribution at the working conditions, which is detailed in the experimental procedure subsection. The CFD outcomes closely align with the experimental data, corroborating the isothermal expansion hypothesis, as the CFD model assumes uniform mixture temperature.



117

Figure 2. Pressure distribution comparison between the measured, simulated, and designed values

118

119

Subsequently, we employ the polytropic index to gauge the extent to which this process approximates a strictly isothermal expansion. To quantify the polytropic index, we apply the energy conservation equation to the nozzle's outlet, where the pressure is P , and the mixture's velocity is expressed by:

120

121

122

123

$$u^2 = \frac{2\dot{V}_w(P_{inj} - P)}{\dot{m}_w + \dot{m}_a} + u_{inj}^2 + \frac{2}{\dot{m}_w + \dot{m}_a} \times (\dot{W}_a - \dot{E}_{loss}) \quad (1)$$

where \dot{V}_w , P_{inj} , \dot{m}_a , \dot{m}_w , u_{inj} , \dot{W}_a and \dot{E}_{loss} are the water volumetric flow rate, air injection pressure, air mass flow rate, water mass flow rate, water injection velocity, work rate exerted by air, and energy losses, respectively. Further discussion on the governing equations can be found in the experimental procedure section. The air expansion work is assumed to be a polytropic process, for which the work rate is calculated by¹²:

124

125

126

127

128

$$\dot{W}_a = P_{inj} \dot{V}_{a,inj} \frac{1 - \left(\frac{P_{inj}}{P_{out}}\right)^{\frac{1-n}{n}}}{n - 1} \quad (2)$$

where n and P_{out} are the polytropic index and the outlet pressure, respectively. As a result, equation 1 involves two unknown variables: the polytropic index and the head losses in the nozzle.

129

130

131

To gain insights on the head losses in the nozzle, we evaluate the expression $\dot{E}_{loss} = \dot{V}_w \Delta P$, where ΔP is the pressure loss, and is calculated by $\Delta P = \zeta \frac{\rho u^2}{2}$. Here, ζ , ρ , and u are the resistance coefficient, mixture's density and inlet velocity, respectively²⁷.

132

133

134

In the above equation, ζ depends on geometrical factors while the term ρu^2 strongly depends on the void fraction and, thus, the temperature and the polytropic index. Consequently, compre-

135

136

hending the influence of the polytropic index on this parameter is sufficient to infer the nuzzle's head loss characteristics. This relationship is quantified by the equation below:

$$\rho u^2 = [\alpha \rho_a + (1 - \alpha) \rho_w] \times \frac{\dot{V}_w^2}{A^2 (1 - \alpha)^2} = \frac{\dot{V}_w^2}{A^2} \times \left[\frac{\alpha \rho_a}{(1 - \alpha)^2} + \frac{\rho_w}{1 - \alpha} \right], \quad (3)$$

where α is the void fraction and A is the cross-sectional area. Figure 3 plots the above term as a function of the polytropic index using the measured conditions at the nozzle's outlet. The head losses monotonically reduce with increasing the polytropic index, indicating that the largest head losses are received for the pure isothermal case. Therefore, the head losses obtained from the CFD simulation, representing perfect heat transfer between the phases, can be considered an upper bound for the actual head loss.

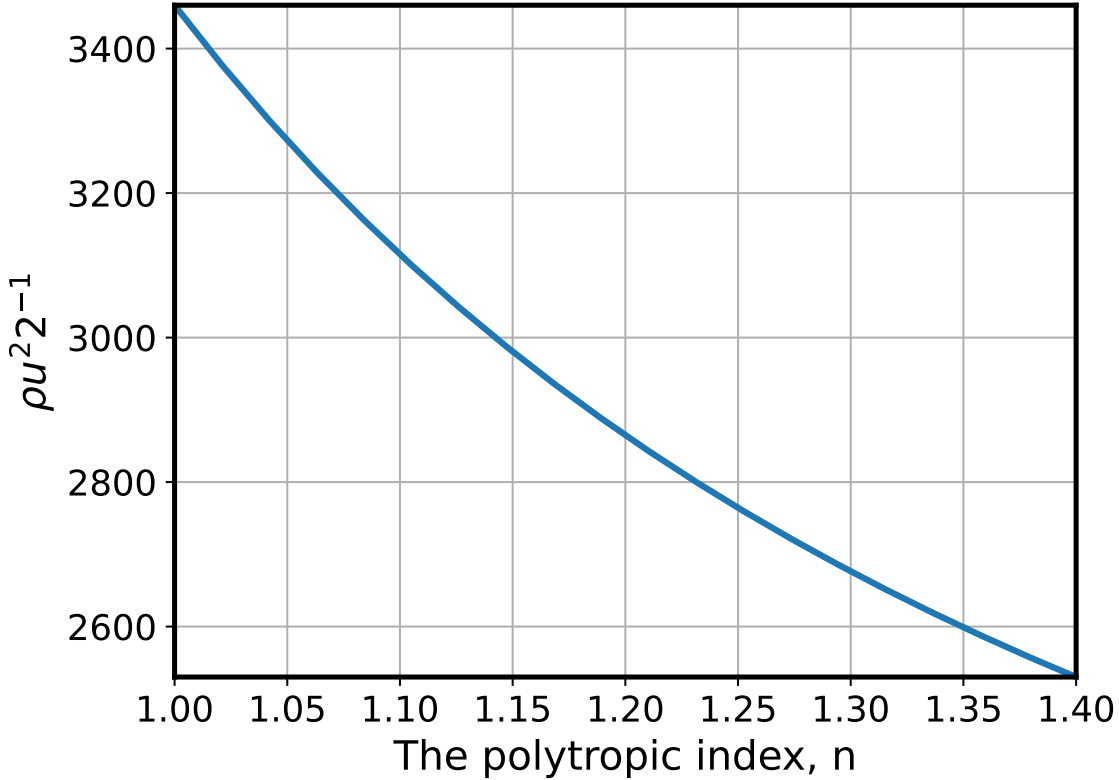
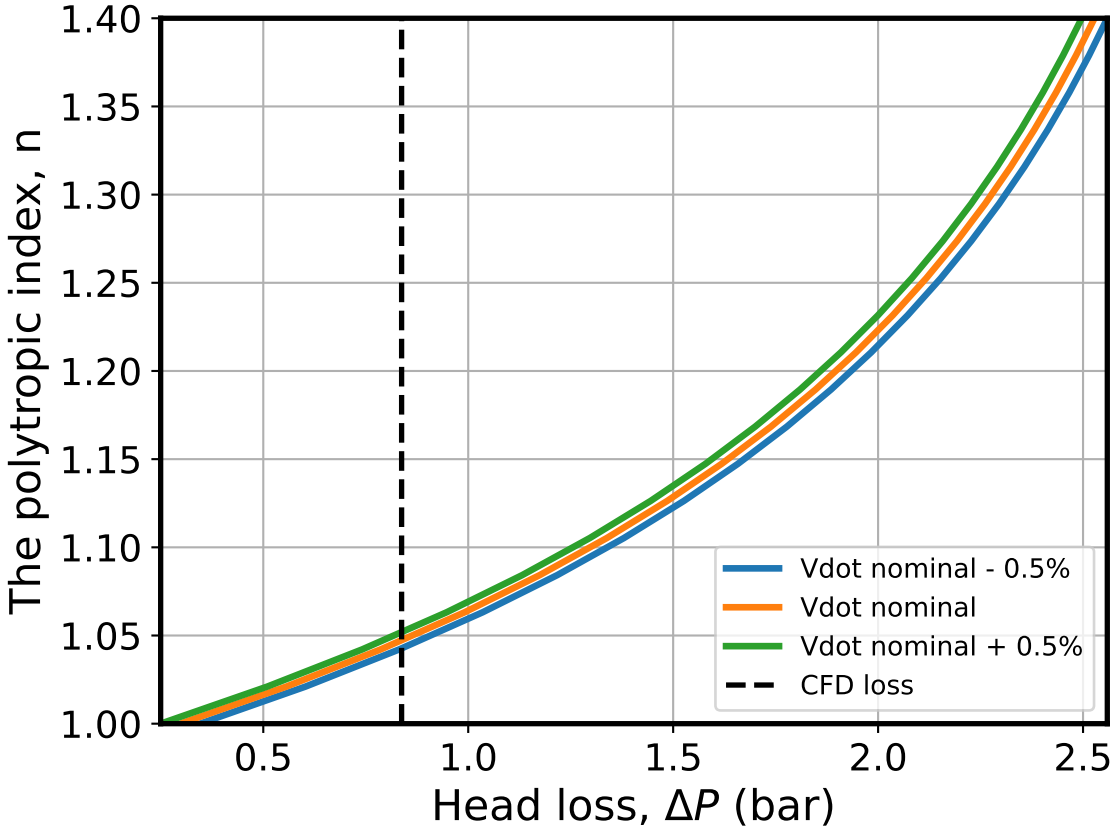


Figure 3. Head loss dependence on the polytropic index

In Figure 4, we plot the solution for the energy conservation equation (equation 1) for the nominal conditions and water volumetric flow rates error of 0.5%. Since both head losses and n are unknown, each point on this curve is a solution to this equation. Using the head losses found in the CFD simulation of 0.56 bar as an upper bound to our experiment, we can extract an upper bound on the polytropic index, n . From this analysis, the upper bound for the polytropic index is 1.032.



153

Figure 4. Solution to equation 1 using measured data.

154

One of the benefits of isothermal expansion stems from the additional work that can be extracted in the expansion process. Hence, It is instructing to understand the improved extracted work compared to the adiabatic process, which represents gas expansion with no heat exchange. Therefore, we define the isothermal efficiency by the ratio between the polytropic-index dependent work, $\dot{W}_a = P_{inj} \dot{V}_{a,inj} \frac{1 - (\frac{P_{inj}}{P_{out}})^{\frac{1-n}{n}}}{n-1}$, and the isothermal work $\dot{W}_{iso} = P_{inj} \dot{V}_{a,inj} \ln \left(\frac{P_{inj}}{P_{out}} \right)$ ¹²:

155

156

157

158

159

$$\eta_{iso} = \frac{\dot{W}_a}{\dot{W}_{iso}} = \frac{1 - r_p^{\frac{1-n}{n}}}{(n-1)\ln(r_p)}, \quad (4)$$

where P_{out} is the outlet pressure and $r_p = \frac{P_{inj}}{P_{out}}$ is the pressure ratio.

160

Figure 5 shows the isothermal efficiency using the extracted polytropic index of $n = 1.032$ for pressure ratios up to 10, for which isothermal efficiencies $> 94\%$ are attained. As such, an additional 46-78 % more work can be extracted compared to adiabatic expansion, for which $n = 1.4$. In the context of heat engines using organic working fluids, these are associated with a lower polytropic index of $n = 1.05 - 1.3$. As such, increasing work extraction by approaching isothermal expansion is limited and dependent on the polytropic index of the working fluid.

161

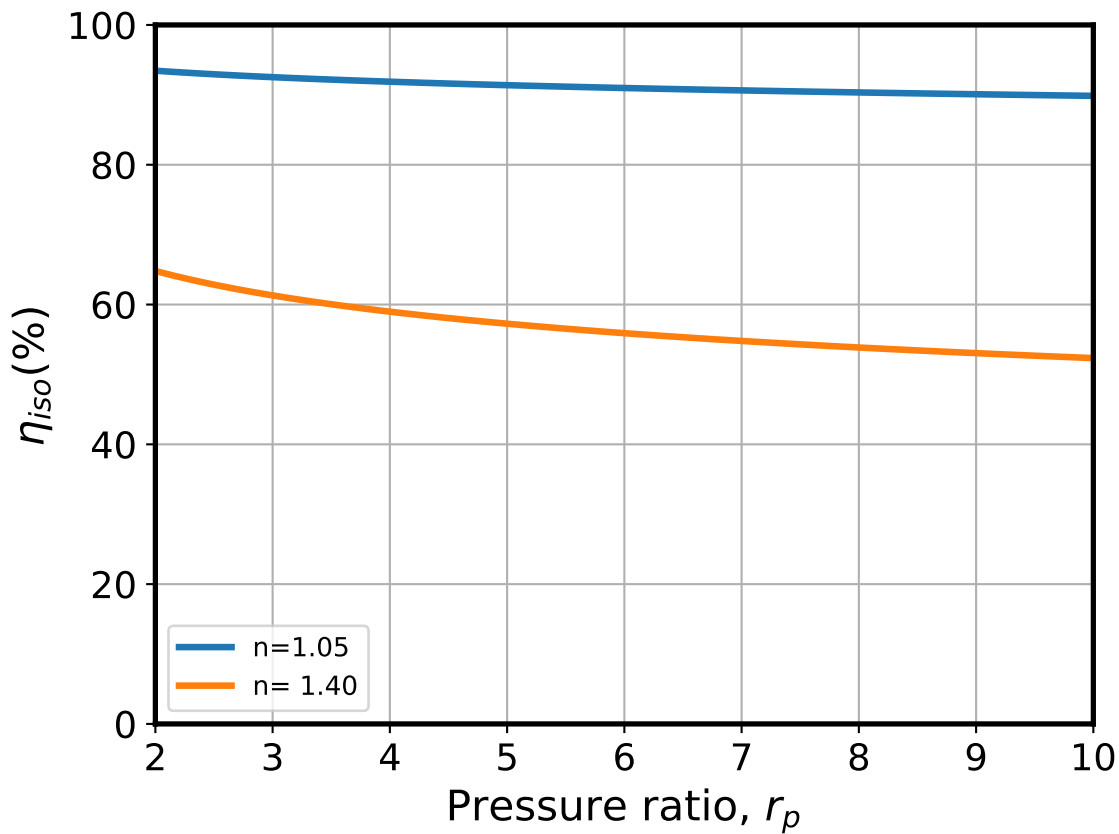
162

163

164

165

166



167

Figure 5. Isothermal efficiency for varying pressure ratios.

168

High impeller efficiency

169

The near-isothermal expansion of bubbles experienced in our nozzle reveals opportunities for a new type of heat engine utilizing such nozzles for a reaction turbine. The turbine consists of an impeller connected to nozzles. The rotor leg is submerged in the HTL reservoir, sucking HTL into the rotor. Similarly to a centrifugal pump impeller, the impeller vanes pressurize the HTL until reaching maximal static pressure at the end of the impeller, where the nozzles begin, and liquid WF is injected and mixed with the HTL. However, unlike the centrifugal pump, our impeller has no stator, which minimizes energy losses while maintaining high design flexibility. In the nozzles, heat is transferred from the HTL to the WF until the WF is fully evaporated, and the mixture is accelerated until it reaches the nozzles' outlet, where the jet flows tangentially, creating a thrust force and rotates the shaft for electricity generation. An example of the impeller design is shown in Figure 6.

170

171

172

173

174

175

176

177

178

179

180

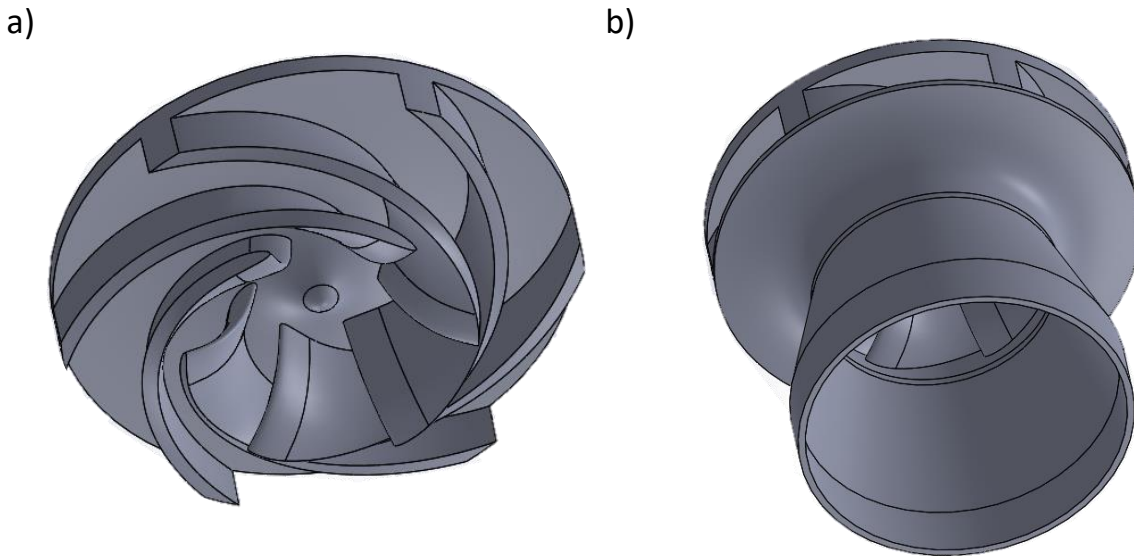


Figure 6. Impeller design. (a) hidden shroud, and (b) with shroud.

Figure 7 exemplifies CFD simulation of an impeller design for 10.5 bar injection pressure, resulting in an impeller efficiency of $\sim 97\%$.

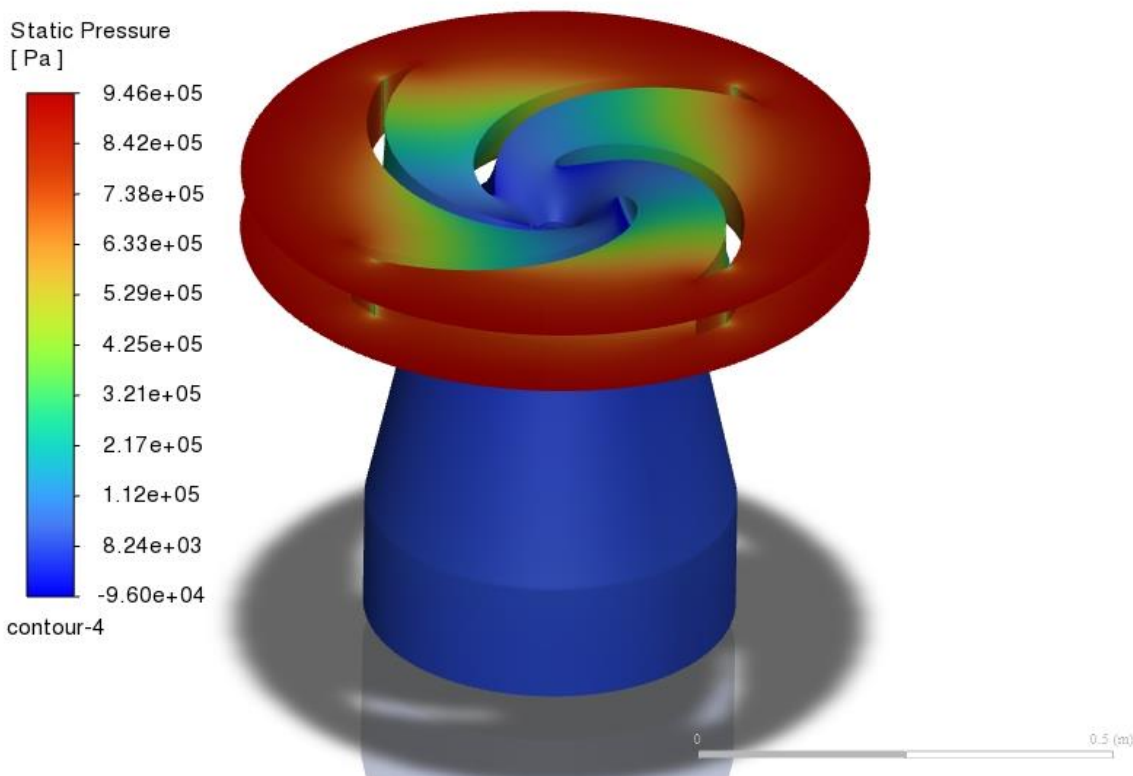


Figure 7. CFD results of the impeller at 1500 RPM. Pressure values are written in bar gauge.

Description of the ISO cycle

This subsection details the novel thermodynamic cycle (ISO cycle henceforth), where the WF undergoes phase changes and an isothermal expansion for work extraction. We simulate a phase-changing cycle to enable apples-to-apples comparison to the organic Rankine cycle, where the

heat source is saturated steam. In this cycle, depicted in Figure 8, the HTL transfers thermal energy from an outside heat source to the WF for evaporation and expansion, while the WF performs work on the HTL, rotating a reaction turbine, ultimately generating electricity. The heat source passes through a heat exchanger (1→2), which transfers heat to the HTL (4→5). Since heat is added to the HTL quasi-isothermally, the heat source leaves the heat exchanger at a high temperature. As such, it is further utilized in an additional heat exchanger (2→3), preheating the WF. The HTL is pumped by the turbine in conjunction with colder HTL from the reservoir (6). The HTL flow from the reservoir is used to obtain the desired HTL flow rate in the nozzle, resulting in a specific void fraction. Before reaching the nozzle, the impeller increases the HTL's pressure to the WF's saturation pressure. The HTL reaches the nozzle's inlet and mixes with colder WF liquid (7) in the nozzle's injection chamber. Heat transfers to the WF, which raises its temperature to its evaporation temperature. The WF then completely evaporates and expands inside the nozzle within the HTL until it reaches its outlet (8). This expansion raises the mixture's velocity and generates thrust, which turns the reaction turbine. The rotor rotates in a tank that functions as a vertical vapor-liquid separator, separating the WF from the HTL after the expansion. The hot WF gas enters a recuperator, which transfers heat from the hot WF to the cold condensed WF before it enters the condenser (9→10). This internal regeneration, facilitated by the isothermal expansion, is used to heat the cold liquid WF, minimizing heat transfer irreversibilities. Then, the liquid WF is pumped through the recuperator (11→12). The WF is pre-heated using the heat source (12→13), transferring more heat from the still-hot heat source. The WF is then injected into the nozzles, mixing with the hot HTL (7).

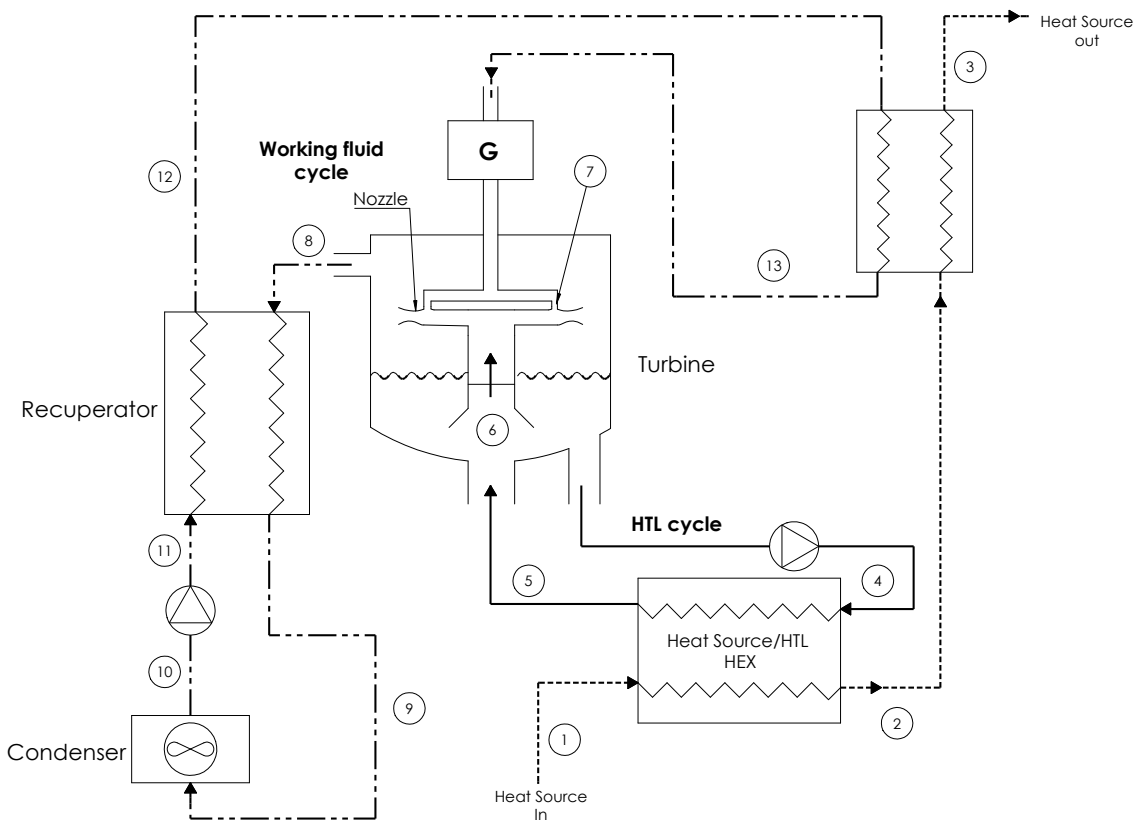


Figure 8. Schematic of the ISO cycle.

The ISO cycle was simulated for source temperatures of 100-190 °C with N-pentane as the WF and Ethylene glycol as the HTL. N-pentane is chosen due to its high critical temperature of 196.7 °C, condensation at near atmospheric conditions, meager global warming potential, and

zero ozone depletion potential²⁸. The thermophysical properties of the materials were acquired from the National Institute of Standards and Technology (NIST) REFPROP database²⁹.

The ISO cycle simulation is based on the following assumptions:

- The HTL is incompressible.
- Ideal mixture and equilibrium between the phases in the nozzle.
- Perfect phase separation after expansion.

ISO cycle performance analysis

Saturated steam is chosen as the heat source, representing a condensation scenario that facilitates high efficiency due to a high-temperature working point and high power output by harnessing a large amount of latent heat. For low-grade heat sources, the latent heat is the primary factor of the internal energy of the source (e.g., latent heat is >70% of steam's energy in temperatures <180°C). This application is optimally suited for the ISO cycle, as the predominant portion of the heat involved is latent heat, allowing significant heat extraction with minimal temperature change.

To understand the benefit of the proposed cycle, we compare its performance to a conventional recuperated ORC. In the simulated ORC cycle, the WF is heated in a boiler by the same heat source and expands in a turbine. Then, the colder WF transfers heat by a recuperator before it condenses and is pumped back into the boiler through the recuperator. In the two cycles, the temperature of the hot WF is optimized to extract maximum power. Figure 9 exemplifies T-S diagrams of the two cycles using heat source temperature (T_H) of 150 °C. The differences between the cycles are visible in the additional heat extracted by the ISO cycle compared to maintaining isothermal expansion.

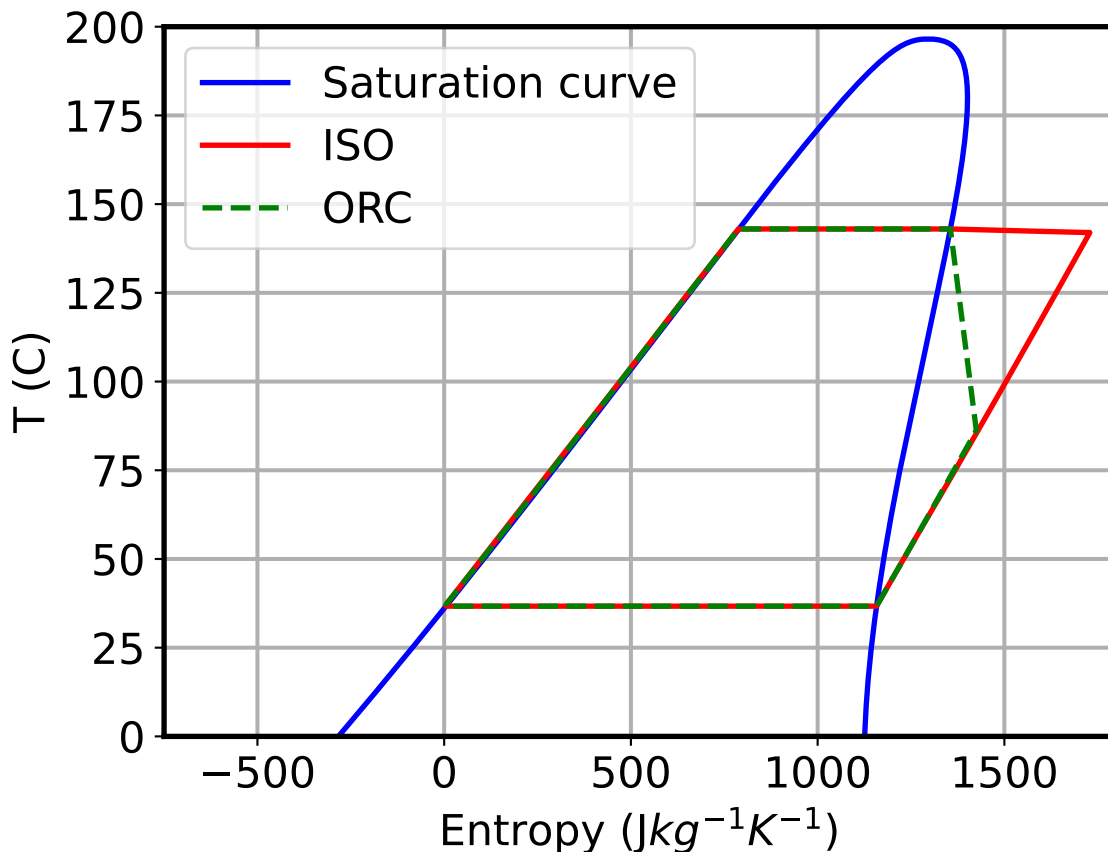
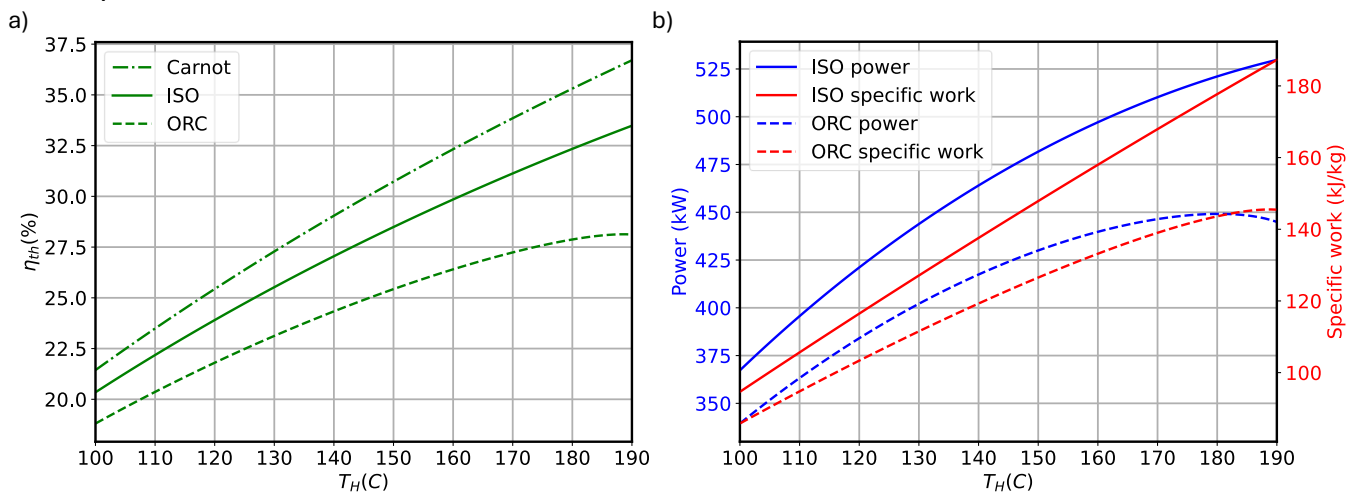


Figure 9. T-S diagrams of the compared cycles at $T_H = 150^\circ C$.

241

First, we compare the efficiency and power output of an ideal ISO cycle to an ideal organic Rankine cycle using the same heat inputs and working fluids. Figures 10 a and b show that the ISO cycle outperforms ORC in both efficiency and power output metrics, respectively. The gains in power output are tabulated in Table 1, showing that the ISO cycle can extract up to 19% more power than the ideal ORC. The enhanced efficiency is achieved through isothermal expansion, reducing irreversible heat transfer. In terms of the specific work, which is the power divided by the WF's mass flow rate, the improvement is more profound, reaching 29% at the temperature of $190^\circ C$. This results from a higher WF mass flow rate allowed by the ORC cycle. The second law efficiency of the proposed cycle is 91.5%-94.5%, approaching the Carnot efficiency, compared to $<88\%$ using the ORC. The power generated by the ORC heat engine peaks at $180^\circ C$ and reduces afterward. This reduction is due to diminished thermal input at elevated temperatures, resulting from the steam's latent heat decreasing as temperature rises. This phenomenon is absent in the ISO cycle because the efficiency gains at higher temperatures offset the decline in heat input.

255



256

Figure 10. Comparative analysis between the ISO cycle and ORC of efficiencies (a) and net output work (b).

257
258

Table 1. ISO cycle improvement

259

T_H	Power output improvement	Specific work improvement
(°C)	(%)	(%)
100	8	10
110	9	11
120	10	13
130	10	14
140	11	15
150	12	17
160	13	19
170	14	21
180	16	24
190	19	29

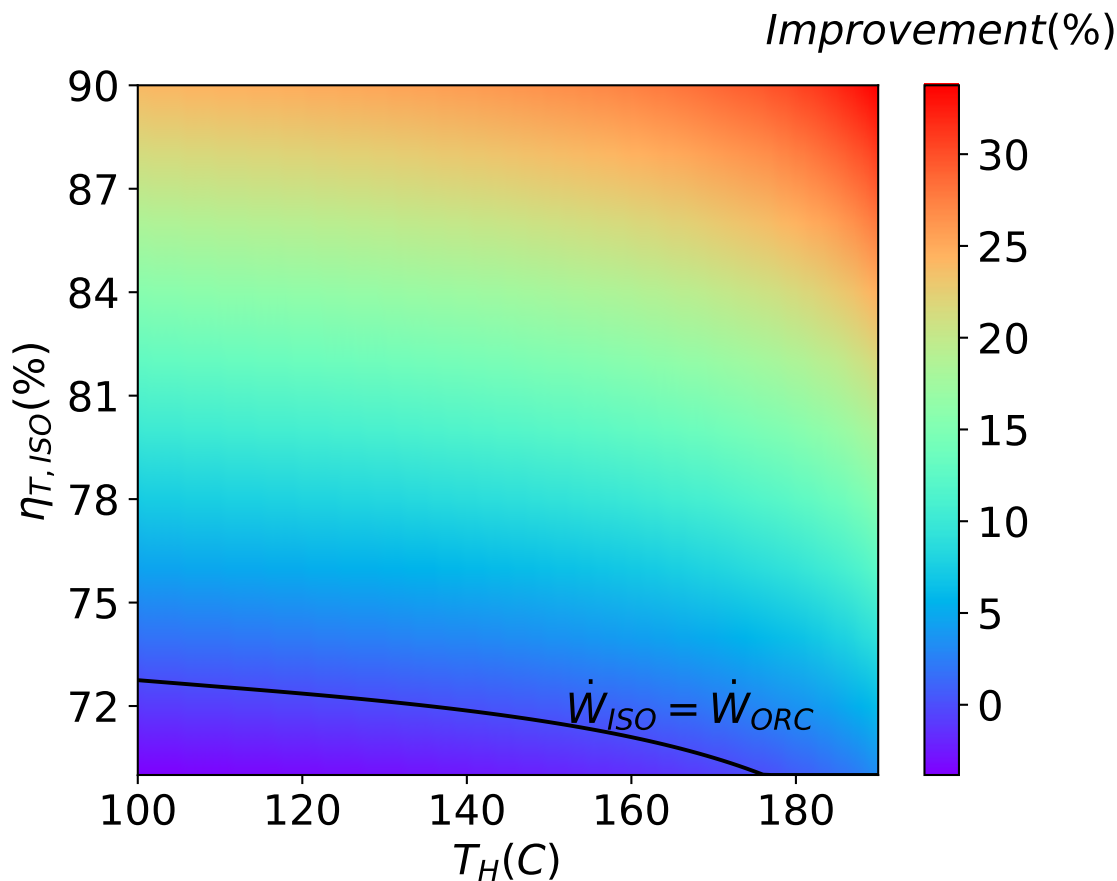
260

Next, we compare a more realistic scenario in which the cycles' inefficiencies are integrated into the simulation. Table 1 summarizes parameters applied in both cycles during the simulation, while the experimental procedure section further details the mathematical analysis of the ISO cycle. The scale of the system is a few hundred kW, which is the scale needed for many industrial waste heat recovery systems. In this scale, the ORC turbine efficiency is considered as 75%, similar to the value considered by previous studies⁴.

261
262
263
264
265
266

Since the reaction turbine has yet to be built and experimented with, we consider turbine efficiencies in the range of 70-90%, where the ISO turbine efficiency is defined by the ratio of the turbine output power to the WF expansion work. Figure 11 illustrates the output power enhancement of the ISO cycle across the varying turbine efficiencies relative to the ORC, considering a realistic ORC expander exhibits isentropic efficiency of 75%, consistent with values used in past studies⁴. The black curve in the figure denotes the ISO turbine efficiency for which the output power of the two cycles is equal. The figure indicates that in the considered ISO turbine efficiency, the ISO cycle potentially generates up to 33.8% more power than the ORC-based heat engine.

267
268
269
270
271
272
273
274
275



276

Figure 11. ISO cycle improvement compared to the ORC as a function of the heat source temperature and the ISO turbine efficiency considering ORC turbine isentropic efficiency of 75%. The black curve denotes the ISO turbine efficiency for which the ISO cycle and ORC produce equal power.

277

278

279

280

When applied to ideal gas cycles, such as the Ericsson cycle, the proposed turbine may offer even higher-efficiency heat engines. There is no phase change in this cycle, and the gas undergoes isothermal compression, theoretically approaching Carnot's efficiency. Thus, the successful implementation of effective isothermal compression could pave the way for developing heat engines with efficiencies surpassing those achievable by the ISO cycle.

281

282

283

284

285

Conclusions

286

This study introduces the concept of a supersonic two-phase nozzle as a key component of a novel thermodynamic phase-change cycle utilizing isothermal expansion. Experimental pressure measurements with air in water validated the supersonic conditions, while CFD allowed us to extract an upper bound for the polytropic index of air of $n < 1.052$. This index indicates quasi-isothermal expansion, enabling up to 75% more work extraction than adiabatic expansion. Compared to other reported methods, such as flooded expansion, this method achieves a much higher liquid-to-working-fluid mass ratio (0.997 compared to 0.3). This significantly increases the heat transfer between the phases, enabling almost isothermal gas expansion. Furthermore, using the two-phase nozzle is an important step for increasing the pressure ratio, which makes it more suitable for various applications.

287

288

289

290

291

292

293

294

295

296

To leverage this nozzle for realizing a heat engine, we theoretically explored a reaction turbine, which rotates due to thrust created by the nozzles. CFD analysis of the impeller shows hydraulic efficiency of $\sim 97\%$ supporting its efficiency potential compared to existing small-scale turbines. 297
298
299
300

The suggested turbine was simulated for a new heat engine (ISO cycle). The ISO cycle yielded superior performance compared to a conventional ORC cycle and showed up to 19% higher power output for heat source temperatures up to 190°C . 301
302
303

We broadened our simulation to encompass ISO turbine efficiencies spanning from 70% to 90% and compared to ORC small-scale heat engine, which encompasses turbine isentropic efficiency of 75%. This analysis revealed that the ISO cycle outperforms the ORC within the examined temperature range when turbine efficiency exceeds 73%. 304
305
306
307

Not only is it more efficient, but the ISO turbine has the potential to be much smaller than an ORC counterpart. This is because the energy carrier in the ISO cycle is liquid, three orders of magnitude denser than gas, which is the typical energy carrier in ORC and other heat engines. 308
309
310

Future research should focus on building and experimentally validating the proposed cycle, optimizing its components, and exploring its potential applications in various energy systems. 311
312

Experimental procedures

313

Governing expressions for the energy conservation equation

314

The air expansion is assumed to be a polytropic process, for which the work rate is calculated by¹²:

315

316

$$\dot{W}_a = P_{inj} \dot{V}_{a,inj} \frac{1 - \left(\frac{P_{inj}}{P}\right)^{\frac{1-n}{n}}}{n - 1} \quad (5)$$

where n is the polytropic index. Specifically, in adiabatic conditions, the polytropic index equals the ratio of the specific heats (1.4 for air) and $n = 1$ for isothermal expansion. The work rate for isothermal expansion is determined by:

317

318

319

$$\dot{W}_{iso} = P_{inj} \dot{V}_{a,inj} \ln \left(\frac{P_{inj}}{P} \right). \quad (6)$$

The mixture's velocity can be expressed by:

320

$$u = \frac{\dot{V}_w}{A(1 - \alpha)} \quad (7)$$

where A and α are the cross-section area and the void fraction, respectively. By using the relation of pressure and void fraction²¹:

321

322

$$P = P_{inj} \left[\frac{\alpha_{inj}(1 - \alpha)}{\alpha(1 - \alpha_{inj})} \right]^n \quad (8)$$

and by measuring \dot{V}_w , \dot{m}_a , P_{inj} and P , energy losses \dot{E}_{loss} can be calculated for a given n using equations 1, 5, 7 and 8.

323

324

Nozzle CFD analysis

325

A 3D CFD simulation using the finite volume methods was performed on a nozzle using the commercial solver FLUENT 2024R1. The CFD model was validated by comparing the static pressure results with the experimental measurements along the nozzle. Due to the highly dispersed gas phase in the liquid flow and the high boundary area between phases, a 'Mixture' multiphase model was used. The 'Mixture' multiphase model is a simplified model that treats the mixture as a single continuum without sharp boundaries between the phases. The standard fluid dynamic governing equations are modified by introducing the void fraction parameter. No slip velocity between phases was assumed. A steady Reynolds Averaged Navier-Stokes (RANS) turbulence modeling approach was used to minimize simulation runtime. The RANS approach provides a solution for the time-averaged turbulent flow parameters. Although it eliminates the fluctuating terms, it is a powerful simplification that allows reasonably accurate results under reasonable computation costs. As a closure model, K-omega SST was compared with the K-epsilon models. Both models produced similar results. The simulations were performed with several cell sizes to verify the independence of the results from cell size. Cells used are polyhidara cells. Prism cells were modeled for the wall treatment. A sufficient number of prism cells was assured using the Effective Viscosity Ratio (EVR) parameter, ensuring the actual boundary layer falls within the scope of the prism cells.

326

327

328

329

330

331

332

333

334

335

336

337

338

339

340

341

342

Impeller CFD analysis

343

The impeller is designed and optimized using ANSYS 2024R1 software. For this purpose, a few ANSYS modules were used. We used Vista CPD to define the initial impeller geometry for specific operating conditions, followed by BladeGen to create the final blade, shroud, and hub geometries. In the next step, the fast solver of VistaTF is applied to check operating conditions. Finally, Fluent's full CFD solution is done to evaluate impeller efficiency and $NPSH_r$. The fine mesh with sufficient boundary layer modeling was used, and three levels of mesh refinement validated the convergence. For all meshes, y_+ was less than 1.

344
345
346
347
348
349
350

ISO cycle Simulation model

351

In this subsection, we outline the thermodynamic framework applied to assess the ISO cycle.

352

For each temperature, we solved the following equations:

353

$$1. \dot{m}_{HTL,7} = \dot{m}_{HTL,A} + \dot{m}_{HTL,int}$$

354

$$2. \dot{m}_{HTL,A} = \frac{\dot{m}_{WF} q_{13-8}}{C_{p,HTL} (t_5 - t_4)}$$

355

$$3. \dot{m}_{HTL,int} = \frac{\dot{m}_{WF} (h_7 - h_{13}) + \dot{m}_{HTL,A} C_{p,HTL} (t_7 - t_5)}{C_{p,HTL} (t_8 - t_7)}$$

356

$$4. q_{13-8} = h_7 - h_{13} + t_8 (s_8 - s_7)$$

357

$$5. \alpha_{out} = \frac{\dot{V}_{WF}}{\dot{V}_{WF} + \dot{V}_{HTL}}$$

358

where s , h , t , q , \dot{V} , \dot{m} and C_p are the entropy, enthalpy, temperature, specific heat, volumetric flow rate, mass flow rate, and heat capacity, respectively, and the numbered subscripts denote the thermodynamic cycle points presented in Figure 8. These equations were solved under $\alpha_{out} = 0.74$, representing the maximum void fraction that can sustain a bubbly flow of packed spheres²². This void fraction maximizes power extraction while maintaining high thermal contact between the HTL and the WF, thus ensuring high model accuracy.

359
360
361
362
363
364

For each heat source temperature, we optimize the nozzle's outlet temperature to achieve maximum net power output.

365
366

The thermal efficiency of the cycle is calculated as follows:

367

$$\eta_{th} = \frac{\dot{W}_{net}}{\dot{Q}_{in}}, \quad (9)$$

where \dot{Q}_{in} is the rate heat transferred into the system.

368

The net output work of the heat engine is calculated as:

369

$$\dot{W}_{net} = \dot{W}_T - \dot{W}_{p,WF} - \dot{W}_{p,HTL} - \dot{W}_{fans} \quad (10)$$

where \dot{W}_T , $\dot{W}_{p,WF}$ and $\dot{W}_{p,HTL}$ are the turbine's output work, and the work consumed by the WF and the HTL pumps, respectively. \dot{W}_{fans} is the needed work for the condenser's fans.

370
371

The turbine's output work is calculated as:

372

$$\dot{W}_T = \dot{W}_{exp} \times \eta_{T,ISO} \quad (11)$$

where \dot{W}_{exp} and $\eta_{T,ISO}$ are the expansion work and ISO turbine efficiency, respectively.

373

RESOURCE AVAILABILITY

374

Lead contact

375

Requests for further information and resources should be directed to and will be fulfilled by the lead contact, Dror Miron (drormiron@gmail.com).

376

377

Materials availability

378

This study did not generate new materials.

379

Data and code availability

380

- Any information required to reanalyze the data reported in this paper is available from the lead contact upon request.

381

382

ACKNOWLEDGMENTS

383

The work of D. Miron was supported by the Israel Department of Energy (PhD fellowship) and by the Nancy and Stephen Grand Technion Energy Program (GTEP).

384

385

AUTHOR CONTRIBUTIONS

386

Conceptualization, D.M., Y.N, J.C., and C.R; methodology, D.M., Y.N, J.C., and C.R.; investigation, D.M., Y.N, N.F, A.S, and J.C.; visualization, D.M.; writing—original draft, D.M., Y.N, J.C., and C.R.; writing—review & editing, D.M., Y.N, J.C., A.S, N.F, and C.R.; funding acquisition, C.R.; supervision, C.R.

387

388

389

390

DECLARATION OF INTERESTS

391

All authors are employees and shareholders of Lave power ltd.

392

References

393

1. Masson-Delmotte, V. Global Warming of 1.5°C: An IPCC Special Report on the Impacts of Global Warming of 1.5°C Above Pre-industrial Levels and Related Global Greenhouse Gas Emission Pathways, in the Context of Strengthening the Global Response to the Threat of Climate Chang. World Meteorological Organization (2018).
2. Forman, C., Muritala, I. K., Pardemann, R., and Meyer, B. (2016). Estimating the global waste heat potential. *Renewable and Sustainable Energy Reviews* 57, 1568–1579. doi:<https://doi.org/10.1016/j.rser.2015.12.192>.
3. Geffroy, C., Lilley, D., Perez, P. S., and Prasher, R. (2021). Techno-economic analysis of waste-heat conversion. *Joule* 5, 3080–3096.

394

395

396

397

398

399

400

401

402

4. Bianchi, M., and De Pascale, A. (2011). Bottoming cycles for electric energy generation: Parametric investigation of available and innovative solutions for the exploitation of low and medium temperature heat sources. *Applied Energy* 88, 1500–1509. 403
404
405
5. Guzović, Z., Lončar, D., and Ferdelji, N. (2010). Possibilities of electricity generation in the republic of croatia by means of geothermal energy. *Energy* 35, 3429–3440. URL: <https://www.sciencedirect.com/science/article/pii/S0360544210002434>. doi:<https://doi.org/10.1016/j.energy.2010.04.036>. 406
407
408
409
6. Zhai, H., An, Q., Shi, L., Lemort, V., and Quoilin, S. (2016). Categorization and analysis of heat sources for organic rankine cycle systems. *Renewable and Sustainable Energy Reviews* 64, 790–805. URL: <https://www.sciencedirect.com/science/article/pii/S1364032116303082>. doi:<https://doi.org/10.1016/j.rser.2016.06.076>. 410
411
412
413
7. Ziviani, D., Groll, E. A., Braun, J. E., De Paepe, M., and van den Broek, M. (2018). Analysis of an organic rankine cycle with liquid-flooded expansion and internal regeneration (ORCLFE). *Energy* 144, 1092–1106. URL: <https://www.sciencedirect.com/science/article/pii/S0360544217319576>. doi:<https://doi.org/10.1016/j.energy.2017.11.099>. 414
415
416
417
8. Li, X., Lecompte, S., Van Nieuwenhuyse, J., Couvreur, K., Tian, H., Shu, G., De Paepe, M., and Markides, C. N. (2021). Experimental investigation of an organic rankine cycle with liquid-flooded expansion and r1233zd(e) as working fluid. *Energy Conversion and Management* 234, 113894. URL: <https://www.sciencedirect.com/science/article/pii/S0196890421000716>. doi:<https://doi.org/10.1016/j.enconman.2021.113894>. 418
419
420
421
422
9. Castelli, A. F., Elsidio, C., Scaccabarozzi, R., Nord, L. O., and Martelli, E. (2019). Optimization of organic rankine cycles for waste heat recovery from aluminum production plants. *Frontiers in Energy Research* 7. URL: <https://www.frontiersin.org/articles/10.3389/fenrg.2019.00044>. doi:10.3389/fenrg.2019.00044. 423
424
425
426
10. Nemati, A., Nami, H., Ranjbar, F., and Yari, M. (2017). A comparative thermodynamic analysis of orc and kalina cycles for waste heat recovery: A case study for cgam cogeneration system. *Case Studies in Thermal Engineering* 9, 1–13. URL: <https://www.sciencedirect.com/science/article/pii/S2214157X16300673>. doi:<https://doi.org/10.1016/j.csite.2016.11.003>. 427
428
429
430
431
11. Wang, J., Yan, Z., Wang, M., Li, M., and Dai, Y. (2013). Multi-objective optimization of an organic rankine cycle (orc) for low grade waste heat recovery using evolutionary algorithm. *Energy Conversion and Management* 71, 146–158. URL: <https://www.sciencedirect.com/science/article/pii/S0196890413001714>. doi:<https://doi.org/10.1016/j.enconman.2013.03.028>. 432
433
434
435
436
12. Igobo, O. N., and Davies, P. A. (2014). Review of low-temperature vapour power cycle engines with quasi-isothermal expansion. *Energy* 70, 22–34. 437
438
13. Woodland, B. J., Braun, J. E., Groll, E. A., and Horton, W. T. (2014). Organic rankine cycle with flooded expansion and internal regeneration. Google Patents. , US Patent 8,667,797. 439
440
14. Woodland, B. J., Krishna, A., Groll, E. A., Braun, J. E., Horton, W. T., and Garimella, S. V. (2013). Thermodynamic comparison of organic rankine cycles employing liquid-flooded expansion or a solution circuit. *Applied Thermal Engineering* 61, 859–865. URL: <https://www.sciencedirect.com/science/article/pii/S1359431113003815>. doi:<https://doi.org/10.1016/j.applthermaleng.2013.05.020>. 441
442
443
444
445

15. Van Nieuwenhuysse, Jera and Lecompte, Steven and Couvreur, Kenny and Ziviani, Davide and De Paepe, Michel (2020). Commissioning and preliminary experimental investigation of an organic rankine cycle set-up with oil-flooded expansion. In: R., Yokoyama, ed. 33rd International Conference on Efficiency, Cost, Optimization, Simulation and Environmental Impact of Energy Systems (ECOS 2020). ECOS 2020 Organizing Committee. ISBN 9781713814061 (879–888). 446
447
448
449
450
451
16. Lemort, V., Bell, I., Groll, E. A., and Braun, J. Analysis of liquid-flooded expansion using a scroll expander (2008). 452
453
17. jie FU, Y., jie WEI, Y., and zhong ZHANG, J. (2009). Parametric study on the thrust of bubbly water ramjet with a converging-diverging nozzle. *Journal of Hydrodynamics, Ser. B* 21, 591–599. URL: <https://www.sciencedirect.com/science/article/pii/S1001605808601894>. doi:[https://doi.org/10.1016/S1001-6058\(08\)60189-4](https://doi.org/10.1016/S1001-6058(08)60189-4). 454
455
456
457
18. Zhang, J., Xia, Z., Huang, L., and Ma, L. (2018). Power cycle analysis of two-phase underwater ramjet. *Applied Ocean Research* 71, 69–76. 458
459
19. Gany, A. (2018). Innovative concepts for high-speed underwater propulsion. *International Journal of Energetic Materials and Chemical Propulsion* 17. 460
461
20. Wu, X., Choi, J.-K., Nye, A. L., and Chahine, G. L. (2015). Effect of nozzle type on the performance of bubble augmented waterjet propulsion. In: *Proceedings of the 4th International Symposium on Marine Propulsors (SMP'15)*, Austin, TX, USA. (122–134). 462
463
464
21. Singh, S., Fourmeau, T., Choi, J.-K., and Chahine, G. L. (2014). Thrust Enhancement Through Bubble Injection Into an Expanding-Contracting Nozzle With a Throat. *Journal of Fluids Engineering* 136. 465
466
467
22. Albagli, D., and Gany, A. (2003). High speed bubbly nozzle flow with heat, mass, and momentum interactions. *International Journal of Heat and Mass Transfer* 46, 1993–2003. 468
469
23. Thang, N., and Davis, M. (1979). The structure of bubbly flow through venturis. *International Journal of Multiphase Flow* 5, 17–37. URL: <https://www.sciencedirect.com/science/article/pii/030193227990003X>. doi:[https://doi.org/10.1016/0301-9322\(79\)90003-X](https://doi.org/10.1016/0301-9322(79)90003-X). 470
471
472
24. Mor, M., and Gany, A. (2004). Analysis of Two-Phase Homogeneous Bubbly Flows Including Friction and Mass Addition . *Journal of Fluids Engineering* 126, 102–109. doi:10.1115/1.1637628. 473
474
475
25. Wang, Y.-C., and Chen, E. (2002). Effects of phase relative motion on critical bubbly flows through a converging–diverging nozzle. *Physics of Fluids* 14, 3215–3223. 476
477
26. Furuichi, N., and Terao, Y. (2015). Static pressure measurement error at a wall tap of a flow nozzle for a wide range of reynolds number. *Flow Measurement and Instrumentation* 46, 103–111. 478
479
480
27. Idelchik, I., and Ginevski, A. *Handbook of Hydraulic Resistance*. Begell House (2007). ISBN 9781567002515. URL: <https://books.google.co.il/books?id=YhOmPwAACAAJ>. 481
482
28. Qiu, K., and Entchev, E. (2022). A micro-chp system with organic rankine cycle using r1223zd(e) and n-pentane as working fluids. *Energy* 239, 121826. URL: <https://www.sciencedirect.com/science/article/pii/S0360544221020740>. doi:<https://doi.org/10.1016/j.energy.2021.121826>. 483
484
485
486

29. Lemmon, E. W., Ian H. Bell, M. L. H., and McLinden, M. O. NIST Chemistry WebBook, NIST Standard Reference Database Number 69, Eds. P.J. Linstrom and W.G. Mallard. National Institute of Standards and Technology, Gaithersburg MD, 20899 (2023). 487
488
489